

Role of brittle sigma phase in cryogenic-temperature-strength improvement of non-equi-atomic Fe-rich VCrMnFeCoNi high entropy alloys

Yong Hee Jo, Won-Mi Choi, Seok Su Sohn*, Hyoung Seop Kim, Byeong-Joo Lee, Sunghak Lee

Center for High Entropy Alloys, Pohang University of Science and Technology, Pohang 790-784, Republic of Korea

ARTICLE INFO

Keywords:

High entropy alloy
Thermodynamic calculation
Cryogenic
Mechanical property
Sigma phase

ABSTRACT

An equi-atomic single-fcc-phase CrMnFeCoNi high entropy alloy (HEA) shows much higher tensile properties at cryogenic temperature than at room temperature because of its fcc characteristics and abundant twinning at cryogenic temperature. In order to further improve the cryogenic-temperature tensile properties of single-fcc-phase HEAs, we propose non-equi-atomic Fe-rich VCrMnFeCoNi HEAs, and analyze the strengthening effects of the brittle intermetallic sigma (σ) phase. The σ phase is unintentionally obtained, but favorably shows a pronounced strengthening by its hardness and grain refinement effect due to grain-boundary pinning, which leads to high yield and tensile strengths of 0.76 GPa and 1.23 GPa, respectively, together with good ductility of 54%. This positive utilization of the σ phase is unexpected because its formation has been suppressed in typical HEAs. Our results demonstrate that the present Fe-rich VCrMnFeCoNi design and σ -phase strengthening has potential in high-strength HEA studies.

1. Introduction

Recently, new unique single-phase alloys, *i.e.*, high entropy alloys (HEAs) have been actively developed by alloying five or more elements with a similar element portion [1–4]. These HEAs consist of a single phase of face-centered-cubic (fcc) or body-centered-cubic (bcc), and their properties are varied according to the types and amounts of elements [5–10]. Among these HEAs, an equi-atomic single-fcc-phase CrMnFeCoNi five-element alloy [11] shows much higher tensile properties at cryogenic temperature than at room temperature because of its fcc characteristics and abundant twinning at cryogenic temperature [12–14].

In order to further improve the cryogenic-temperature tensile properties of single-fcc-phase HEAs, various strengthening mechanisms have been intensively studied, such as 1) high lattice distortion and solid-solution hardening due to addition of multi-elements [15,16], 2) grain refinement [17], and 3) precipitation strengthening due to addition of Al, Ti, Mo, and interstitial C [18–22], coupled with deformation twinning. The recent research trends on single-fcc-phase HEAs have widely expanded to include non-equi-atomic compositions [23–29], the addition of small amounts (*e.g.* 5 at% or less) of minor elements [19–22,28], three- or four-element alloy systems [30,31], and precipitation strengthening due to various precipitates [18–20]. That is, HEA designs have deviated from the original definition of single-fcc-phase HEAs. Another important issue is the wide cryogenic applications

of single-fcc-phase HEAs as structural materials, which are fairly limited due to their high cost. Among the major single-fcc-phase elements (Cr, Mn, Fe, Co, and Ni), Fe is a most attractive element under a ‘multi-principal element materials’ condition in which all elements act as principal elements [30,32,33].

In the present study, we propose non-equi-atomic Fe-rich VCrMnFeCoNi HEAs, and analyze the strengthening effects of the σ phase (also a hard phase), to improve cryogenic-temperature tensile properties. Our group reported the cryogenic strength improvement by a partial recrystallization treatment in the VCrMnFeCoNi HEA [34]. Now, we aim to study a microstructure-property relationship on the basis of a appropriated balance of Fe and Mn contents obtained from the reference composition of $V_{10}Cr_{15}Mn_5Fe_{35}Co_{10}Ni_{25}$ (at%). An increase of Fe content by replacing Mn induces a more populated deformation twinning and consequently enhanced strain hardening and ductility because of the increased difference in stability between the fcc and hcp phases. The brittle intermetallic σ phase is unintentionally obtained, in contrast to the thermodynamic calculation data, but favorably shows a pronounced strengthening. Due to the utilization of the σ -phase strengthening as well as deformation twinning in the fcc matrix phase, our HEA shows high yield and tensile strengths of 0.76 GPa and 1.23 GPa, respectively, together with good ductility of 54%. These values are comparable to the tensile properties of the existing HEAs [12–14,19,20,35,36]. Our results demonstrate that this non-equi-atomic Fe-rich VCrMnFeCoNi design has potential in high-strength

* Corresponding author.

E-mail address: bbosil7@postech.ac.kr (S.S. Sohn).

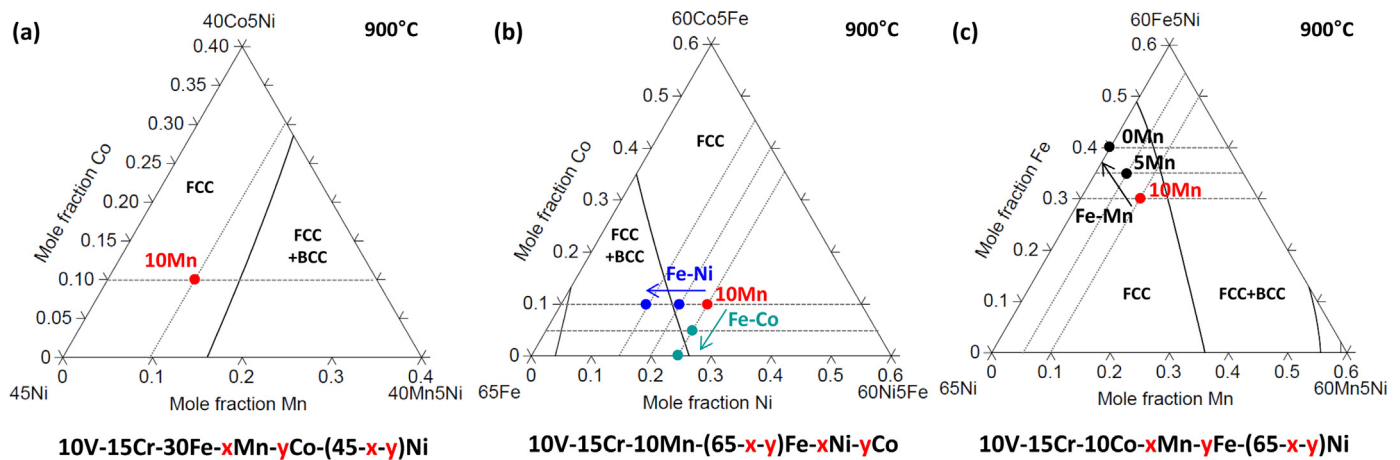


Fig. 1. Equilibrium phase diagrams of 10V-15Cr-xMn-(40-x)Fe-10Co-25Ni alloys designed by thermodynamic calculation. (a) Equilibrium phase diagram obtained when mole fractions of Mn, Co, and Ni are varied at the fixed composition of 10V15Cr30Fe (at%) at 900 °C. (b) equilibrium phase diagram obtained when mole fractions of Fe, Co, and Ni are varied at the fixed composition of 10V15Cr10Mn (at%) at 900 °C. (c) equilibrium phase diagram obtained when mole fractions of Fe, Mn, and Ni are varied at the fixed composition of 10V15Cr10Co (at%) at 900 °C.

HEAs, while fully taking advantages of the excellent HEA properties and σ -phase strengthening, both of which are generally not possible in typical HEAs.

2. Experimental

2.1. Fabrication of 10V-15Cr-xMn-(40-x)Fe-10Co-25Ni HEAs

The three Fe-rich VCrMnFeCoNi HEAs were fabricated using compact vacuum induction melting equipment (model; MC100V, Indutherm, Walzbachtal-Wossingen, Germany) under an argon atmosphere using commercial pure elements (the purity of each raw material was at least 99.9%). Raw elements were alloyed in a ZrO₂-coated alumina crucible to make a master alloy of 150 g in weight. The master alloy was molten at 1500 °C, and was poured into a rectangular graphite module (length = 100 mm, width = 35 mm, thickness = 8 mm). The ingot was encapsulated in evacuated quartz ampules and homogenized at 1100 °C for 6 h. The surface treatment was conducted by a pickling process in a 20% HCl + 80% C₂H₆O solution at room temperature for 10 min to remove scales and contaminants and followed by sand-blasting. The sheet was annealed at 900 °C for 10 min and water-quenched to obtain full recrystallization.

2.2. Microstructural analysis

Microstructures (longitudinal-short-transverse (L-S) plane) of the Villela-etched (100 ml CH₃COOH + 10 ml HCl + 10 ml HClO₄) HEA specimens were observed using a scanning electron microscope (SEM; model JSM-6330F, JEOL, Japan). Phases were identified by X-ray diffraction (XRD, Cu K α radiation, scan rate; 2° min⁻¹, scan step size; 0.02°). Electron back-scatter diffraction (EBSD) analysis (step size; 0.07 μ m) was also conducted using a field emission scanning electron microscope (FE-SEM, Quanta 3D FEG, FEI Company, USA). The EBSD specimens were electro-polished in a 92% CH₃COOH + 8% HClO₄ solution at 32 V. The data were interpreted by orientation imaging microscopy (OIM) analysis software.

2.3. Tensile and nano-indentation tests

Plate-type specimens (gauge length = 6.4 mm, width = 2.5 mm, thickness = 1 mm, longitudinal orientation) were tensioned at room temperature and cryogenic temperature (−196 °C) at a crosshead speed of 6.4×10^{-3} mm/s using a 100-kN-capacity universal testing machine (model; 8801, Instron, Canton, MA, USA). A cryogenic-

temperature chamber (size; 50 × 40 × 38 cm) was installed in the tester for the cryogenic-temperature test. The tensile tests were conducted at least three times for each datum point. Since it was difficult to attach an extensometer inside the low-temperature chamber, the engineering stress-strain curves were calculated from the load-displacement data to compare room- and cryogenic-temperature tensile properties. The elongation of gauge length was measured and calibrated after the testing.

Nano-indentation tests were conducted by using a Hysitron Triolab nano-indentation system (model; PI-85, Hysitron, USA). The hardness of the fcc matrix was measured under a load control at a constant loading rate of 400 μ N s⁻¹ up to a maximum load of 13,000 μ N, while that of the σ phase was measured up to a maximum load of 2000 μ N because the σ phase was very fine below 0.2 μ m. A scanning probe microscope installed in the tester was used to precisely identify the phases. Then, load-displacement curves were obtained and hardness values were calculated using the Oliver-Pharr method [37]. The nano-indentation tests were performed at least ten times for each datum point.

3. Results

3.1. Computational thermodynamic approach for alloy design

The aim of the proposed HEA design for cryogenic applications is to develop cost-effective VCrMnFeCoNi HEAs, and thus the following two key issues are carefully considered. The first issue is preferentially based on large containment of Fe, e.g. 30 at%, in the CrMnFeCoNi system. The vanadium (V) is selected as a new candidate element because it leads to a wide single solid solution in binary phase diagrams with Cr, Fe, or Mn [38]. A larger solid-solution hardening effect might also be expected with the addition of V because the atomic size of V is somewhat larger than that of the other elements. Fifteen at% of Cr is selected for corrosion resistance. In order to theoretically confirm single-fcc-phase equilibrium in the 10V15Cr30Fe system, a computational thermodynamic approach was taken in this study by using Thermo-Calc software [39] together with a database of TCFE2000 and its upgraded version [40–42] because it is a more effective design method than the empirical trial-and-error-based alloy design methods [43–45]. Fig. 1a shows an equilibrium phase diagram obtained when mole fractions of Mn, Co, and Ni are varied at the fixed composition of 10V15Cr30Fe (at%) at 900 °C. The compositions located inside the ‘FCC’ region have a single fcc phase in the range of 900 °C~melting temperature, and the fcc phase is maintained below about 15 at% of

Mn. From the thermodynamic calculation, the basic HEA composition is selected as 10V15Cr10Mn30Fe10Co25Ni (at%).

As the second key issue, for cost-effectiveness, the replacement of Fe by Mn, Co, or Ni is considered to further increase the Fe content inside a single fcc phase. The target Fe content is selected as 40 at% to satisfy the alloy guide and to avoid exceeding 50 at%, i.e. multi-principal element materials condition [7,17]. Fig. 1b shows an equilibrium phase diagram obtained when the mole fractions of Fe, Co, and Ni are varied at the fixed composition of 10V15Cr10Mn (at%) at 900 °C. A single fcc phase is maintained when 5 at% of Ni or Co is replaced with Fe, as represented by a blue or green arrow, respectively, but changes to the two phases (fcc + bcc) when 10 at% of Ni or Co is replaced. Fig. 1c shows a phase diagram obtained when the mole fractions of Fe, Mn, and Ni are varied at the fixed composition of 10V15Cr10Co (at%) at 900 °C. Even when 5 or 10 at% of Fe is replaced by Mn, as marked by a black arrow, the single fcc phase is stably maintained. Based on these three-component phase diagrams, Mn is selected as a competitive element with Fe, and the effects of Mn variation as well as cost-effectiveness are investigated in this study. The three Fe-rich VCrMnFeCoNi alloys, i.e. 0Mn40Fe, 5Mn35Fe, and 10Mn30Fe, are designed at the fixed composition of 10V15Cr10Co25Ni, and are referred to as ‘0Mn’, ‘5Mn’, and ‘10Mn’, respectively, for convenience.

3.2. Microstructures of 10V-15Cr-xMn-(40-x)Fe-10Co-25Ni HEAs

Fig. 2a shows the XRD patterns of the 0Mn, 5Mn, and 10Mn alloys. Only fcc peaks are found in the 0Mn and 5Mn alloys, which indicates that the actual fcc-single-phase microstructures are well matched with those estimated from thermodynamic calculation (Fig. 1c). However, other peaks are observed in the 2 θ range of 38–50°, together with fcc peaks in the 10Mn alloy, as magnified in the inset in Fig. 2a. These peaks are identified as peaks of the σ phase, having a tetragonal crystal structure, which is usually observed in the Fe-Cr, Fe-V, and V-Cr binary systems, the Fe-Cr-Ni ternary system, and austenitic stainless steels [47–51]. In the equi-atomic CrMnFeCoNi HEA, the σ phase is known to be precipitated at 500–700 °C [51]. The presence of the σ phase in the 10Mn alloy does not concur with the thermodynamic calculation data (Fig. 1c), in which the presence of an fcc phase is predicted in these alloys. This is because the database of the σ phase is not sufficiently established for the present 6-component alloy system [40,41,50]. The lattice parameters calculated from the strongest (111) diffraction peak are 0.3596 nm, 0.3601 nm, and 0.3607 nm in the 0Mn, 5Mn, and 10Mn alloys, respectively. The lattice parameters increase as the Mn content increases.

Fig. 2b–d show the EBSD inverse pole figure (IPF) and image quality (IQ) maps of the

(IQ) maps of the three alloys, and their grain sizes are listed above each map (annealing twin boundaries were not counted in the measurements). All the alloys are composed of homogeneously recrystallized fcc grains having annealing twins, and the grain sizes decrease with increasing Mn content. In the IQ map of the 10Mn alloy, a considerable number of particles are observed mostly along grain boundaries. These are the σ -phase particles, as confirmed from the XRD patterns in Fig. 2a.

Fig. 3a and b show an SEM micrograph and energy dispersive spectroscopy (EDS) data of the σ particles present in the 10Mn alloy. The average size and volume fraction of the σ particles are $0.24 \pm 0.11 \mu\text{m}$ and $4.1 \pm 0.5\%$, respectively. The σ particles are distributed mostly along fcc grain boundaries (Fig. 3a). When a σ particle is analyzed along a white-dotted line as shown in Fig. 3a by the EDS, it shows Cr-, V-enriched, and Ni-depleted concentrations (Fig. 3b). Since this σ -phase particle has no definite stoichiometric compositions in the transition-metal alloy systems [46], they might be present in different composition ranges. Thus, the physical properties of the σ -phase particle can be tailored by changing the chemical compositions or by varying the compositional elements within a given structure [46].

3.3. Tensile properties

In typical Fe-Cr-Ni-based alloys, the σ phase is known as a very hard and brittle compound that deteriorates the toughness of the alloy [46,48,49]. It is also the main microstructural factor deteriorating overall properties such as mechanical properties, corrosion resistance, and weldability in stainless steel [49]. In order to understand the effects of σ particle and solid-solution hardening on the matrix, due to the Mn addition, nano-indentation tests were conducted on the fcc matrix and σ particle, the results of which are shown in Table 1. The matrix hardness is highest (4.29 GPa) in the 10Mn alloy, and is similar in the 5Mn and 0Mn alloys. This indicates that the solid-solution hardening effect due to the Mn addition is not clearly visible when the Mn content is less than 10 at%. The hardness of the σ particle is about 24.6 GPa, which is higher than that of the matrix. Since it involves the matrix effect, the actual particle hardness might be higher.

Fig. 4a shows the engineering tensile stress-strain curves tested at room and cryogenic temperatures, from which the yield strength, tensile strength, and elongation were measured, as summarized in Table 1. At both room and cryogenic temperatures, the strengths of the alloys increase with increasing Mn content, while the elongation decreases. The difference in tensile strength between the 0Mn and 5Mn alloys is 24 MPa and 63 MPa at room and cryogenic temperatures, respectively, while that between the 5Mn and 10Mn alloys is 115 MPa and 89 MPa, respectively. The cryogenic-temperature tensile properties are higher in

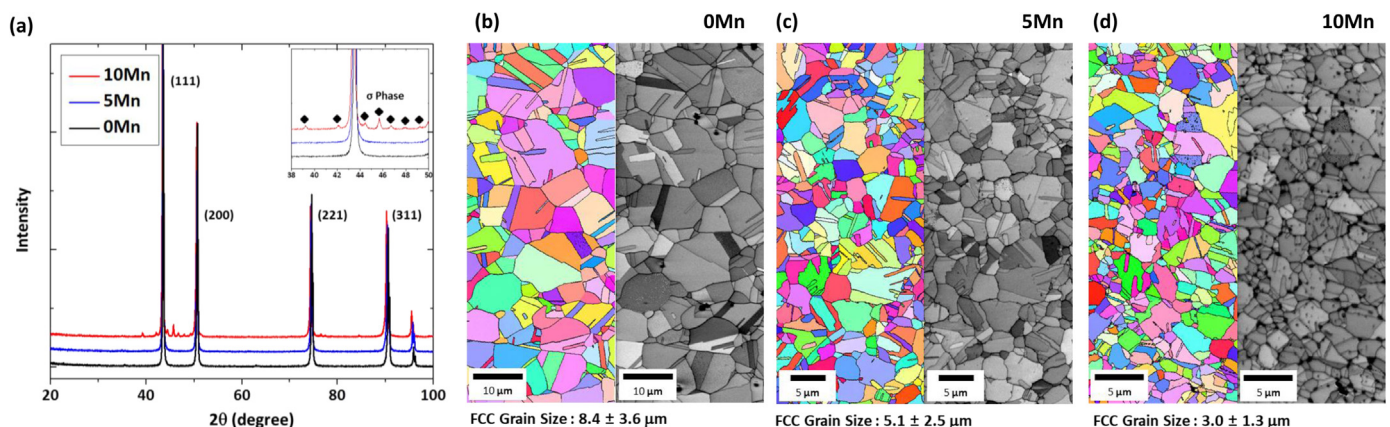


Fig. 2. (a) XRD patterns of the 0Mn, 5Mn, and 10Mn alloys. Only fcc peaks are found in the 0Mn and 5Mn alloys, whereas peaks of σ phase are observed in the 2 θ range of 38–50°, together with fcc peaks, in the 10Mn alloy. EBSD inverse pole figure (IPF) and image quality (IQ) maps of the (b) 0Mn, (c) 5Mn, and (d) 10Mn HEAs. All the alloys are composed of homogeneously recrystallized fcc grains having annealing twins, and grain sizes decrease with increasing Mn content. In the IQ map of the 10Mn alloy, a considerable number of σ -phase particles are observed mostly along grain boundaries.

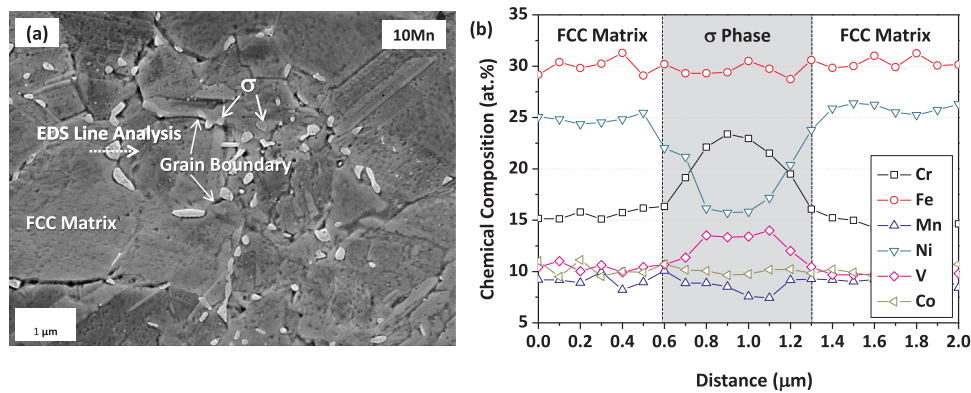


Fig. 3. (a) SEM micrograph showing σ -phase particles in the 10Mn alloy. Most of σ particles of 0.17 μm in average size are distributed along fcc grain boundaries. (b) Energy dispersive spectroscopy (EDS) data of σ particle along a white-dotted line in (a). The σ particle shows a Cr- and V-enriched concentration.

the three alloys than at room temperature, which is typically observed in the fcc HEAs [4,12–14,18,21,50]. Particularly, in the 10Mn alloy, the cryogenic-temperature yield and tensile strengths are highest at 766 and 1225 MPa, respectively, while the elongation remains excellent at 54.1%. Fig. 4b shows the strain-hardening rate curves obtained from the true stress-strain curves. All the alloys show continuously decreasing hardening rate trends. The strain-hardening rate is highest in the 10Mn alloy at both room and cryogenic temperatures below the true strain of 0.25–0.35. This is closely related to the effects of deformation twinning and σ particle on the strain-hardening rate, the details of which will be discussed later.

3.4. Deformation twinning mechanisms

The variation in strength, ductility, and strain hardening with Mn content is closely related to the deformation mechanisms. For fcc HEAs, it has been reported that the main deformation mechanism is the dislocation slip at room temperature, although it changes to the deformation twinning at cryogenic temperature as the resolved shear stress is sufficient to reach the critical stress for twinning [14]. In the alloys in this study, the dislocation slip occurs without any deformation twinning at room temperature. In order to examine the deformation mechanisms at cryogenic temperature, the EBSD analyses were performed on the cross-sectional area beneath the tensile fracture surface, as shown in Fig. 5a–c. In the IQ maps of the three alloys, many parallel lines are observed inside the fcc grains, and are defined as deformation twins having 60° misorientation with the matrix. When these twins develop into a bundle shape, they are clearly visible in the IPF maps. The number of twins decreases as the Mn content increases, which is also confirmed from the misorientation angle distribution data of Fig. 5d–f. Here, boundaries having misorientation angles of 60° are regarded as twin boundaries [13,21,52]. The number fraction of the twin boundary detectable in the IPF maps is highest in the 0Mn alloy

(12%), and decreases in the order of the 5Mn and 10Mn alloys (9% and 5%, respectively).

When considering the relatively lower cryogenic-temperature elongation (54.1%) in the 10Mn alloy than in the 0Mn and 5Mn alloys, the hard σ particles formed along fcc grain boundaries might induce brittle characteristics. Fig. 6a shows an SEM micrograph of the cross-sectional area beneath the cryogenic-temperature tensile-fractured surface of the 10Mn alloy. Void initiation at σ /matrix interfaces and cracking of the σ particles themselves are marked by arrows, although voids or microcracks are not grown or propagated along the grain boundaries. Fractographic observation was conducted on the tensile fracture surface of the 10Mn and 0Mn alloys, as shown in Fig. 6b and c. A ductile dimpled fracture mode prevails in both the 10Mn and 0Mn alloys at cryogenic temperature without intergranular or cleavage modes. In the 10Mn alloy, small σ particles are found inside dimples (Fig. 6b), which indicates that hard grain-boundary σ particles produce ductile dimples because of the very ductile characteristics of the fcc matrix [20].

4. Discussion

Microstructural investigations revealed that the 0Mn and 5Mn alloys are single fcc phase, but the 10Mn alloy contains the σ phase at the fcc grain boundary. Many previous studies have reported the σ phase in the bcc phase ($\text{Al}_{0.3}\text{CrFe}_{1.5}\text{MnNi}_{0.5}$), bcc and fcc dual phase ($\text{Al}_{0.3}\text{CoCr}_2\text{FeNi}$), and fcc phase ($\text{Co}_{0.5}\text{CrFeMn}_{1.5}\text{Ni}$ and CoCrFeMnNi), despite the absence of V. Most alloys showed extremely brittle behavior. The effect of V on the σ phase formation was well investigated by Senkov et al. [53,54] in CoCrFeNiV_x and CoCrFeMnNiV_x alloys. Their mechanical investigation revealed that optimization of the volume fractions of the σ phase through the alloy composition results in good combinations of high strength and good ductility. In relation to the formation rule of the σ phase, the valence electron concentration (VEC)

Table 1

Nano-indentation and room- and cryogenic-temperature tensile test results of the 10V-15Cr-xMn-(40-x)Fe-10Co-25Ni HEAs.

| Temp. | Alloy | Hardness ^a (GPa) | | Yield strength (MPa) | Tensile strength (MPa) | Elongation (%) |
|----------|-------|-----------------------------|----------------|----------------------|------------------------|----------------|
| | | FCC matrix | σ phase | | | |
| 25 °C | 0Mn | 3.9 ± 0.3 | – | 397 ± 1 | 721 ± 7 | 58.0 ± 0.5 |
| | 5Mn | 3.9 ± 0.2 | – | 442 ± 6 | 745 ± 6 | 53.0 ± 0.9 |
| | 10Mn | 4.3 ± 0.3 | 24.6 ± 4.3 | 544 ± 5 | 860 ± 1 | 46.2 ± 0.1 |
| – 196 °C | 0Mn | – | – | 600 ± 13 | 1073 ± 7.5 | 81.4 ± 2.0 |
| | 5Mn | – | – | 698 ± 10 | 1136 ± 10.9 | 78.5 ± 8.8 |
| | 10Mn | – | – | 766 ± 27 | 1225 ± 6 | 54.1 ± 5.0 |

^a The hardness values of fcc matrix and of σ phase were measured up to a maximum load of 13,000 μN and 2000 μN , respectively, at a constant loading rate of 400 $\mu\text{N s}^{-1}$.

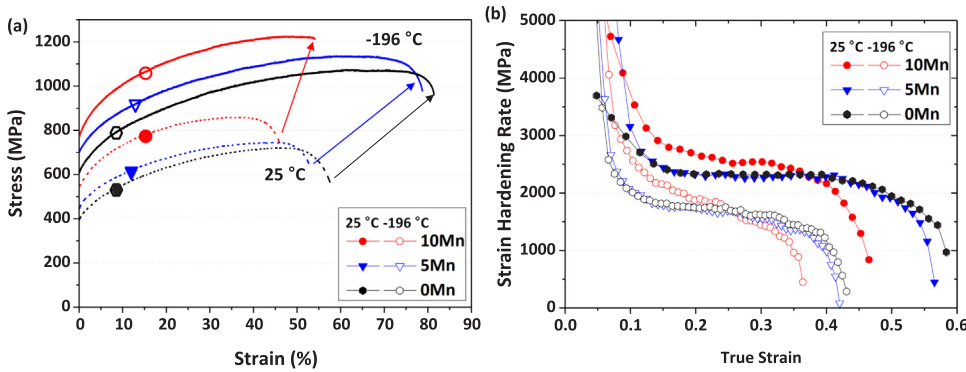


Fig. 4. (a) Room- and cryogenic-temperature engineering stress-strain curves of the 0Mn, 5Mn, and 10Mn alloys. At both room and cryogenic temperatures, the strengths increase with increasing Mn content, while the elongation decreases. At cryogenic temperature, the strengths and elongation are greatly improved over the room-temperature ones. Particularly in the 10Mn alloy, the cryogenic-temperature yield and tensile strengths are highest at 766 MPa and 1225 MPa, respectively, while the elongation is still excellent at 54.1%. (b) Strain-hardening rate curves obtained from true stress-strain curves. The strain-hardening rate is highest in the 10Mn alloy at both room

and cryogenic temperatures below the true strain of 0.25–0.35.

is the most relevant parameter. The atomic size difference is also considered. It is suggested that the σ phase is formed when VEC is in the range of $6.88 < \text{VEC} < 7.84$ [55].

With respect to the thermodynamic calculation, only a single fcc phase is expected at 900 °C in the 10Mn alloy (Fig. 1c). Fig. 7 shows the equilibrium phase fractions of the 10V-15Cr-xMn-(40-x)Fe-10Co-25Ni alloys as a function of Mn content. This calculation implies that the formation temperature of the σ phase is underestimated, considering the formation of the σ phase at 900 °C in the 10Mn alloy. Although the fcc and σ phases region expands as the Mn content increases, it is difficult to consider the fcc and σ phases region for tuning the fraction of the σ phase based on the thermodynamic calculation.

Whether or not the present non-equi-atomic 10V-15Cr-xMn-(40-x)Fe-10Co-25Ni HEAs consists of a single fcc phase can be confirmed by the formation rule using formation parameters such as misfit of atomic radius (δ), configuration entropy (S_{conf}), mixing enthalpy (ΔH_{mix}), and VEC [7–10,26,50]. The calculated parameters along with criteria required for the formation rule in the 0Mn, 5Mn, and 10Mn alloys are summarized in Table 2. All the alloys sufficiently satisfy δ and ΔH_{mix} , while the 0Mn and 10Mn alloys do not satisfy S and VEC, respectively. The S value of the 0Mn alloy is low at 1.46 R because the 0Mn alloy does not have equi-atomic compositions, but the actual microstructure shows a single fcc phase. This indicates that the only entropy term mainly used for the boundary condition of HEAs shows limitations for

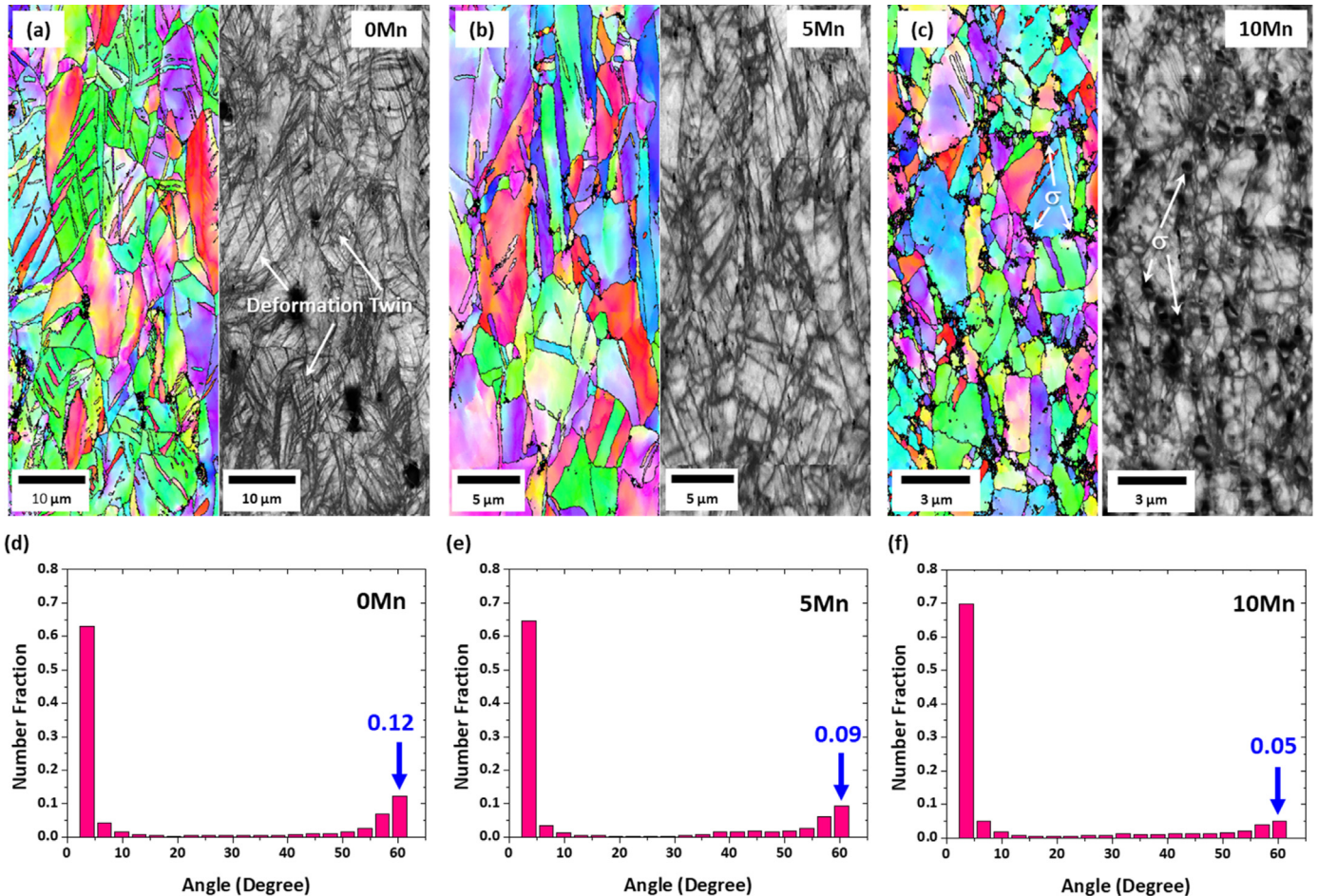


Fig. 5. Cryogenic-temperature tensioned microstructures. EBSD IPF and IQ maps of the cross-sectional area beneath the cryogenic-temperature tensile-fractured surface of the (a) 0Mn, (b) 5Mn, and (c) 10Mn alloys, showing deformation twins. The amount of twins decreases with increasing Mn content. (d–f) misorientation angle distribution data. The number fraction of twin boundary is highest in the 0Mn alloy (12%), and decreases in the order of the 5Mn and 10Mn alloys.

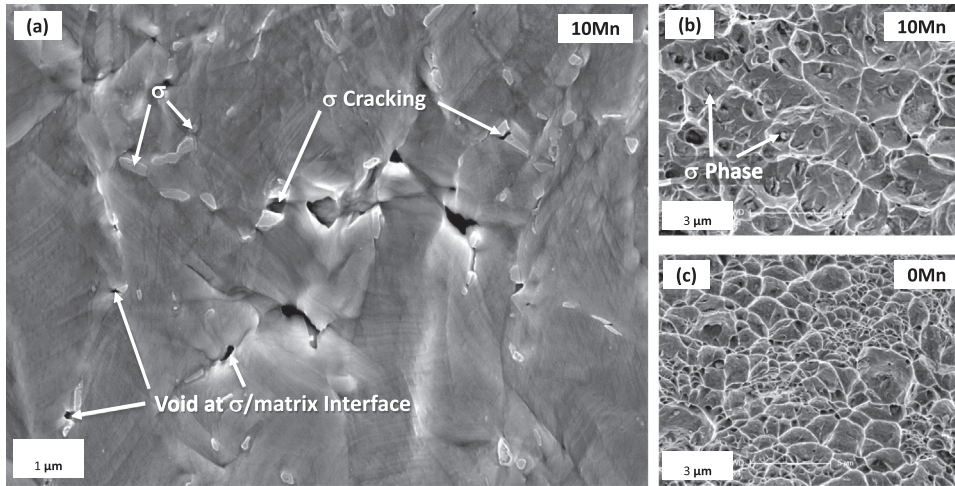


Fig. 6. (a) SEM micrograph of the cross-sectional area beneath the cryogenic-temperature tensile-fractured surface of the 10Mn alloy. A number of voids and cracks are initiated at σ /matrix interfaces and σ particles themselves, respectively, but most of them are not grown along grain boundary. SEM fractographs of the (b) 10Mn and (c) 0Mn alloys. A ductile dimpled fracture mode prevails in both 10Mn and 0Mn alloys at cryogenic temperature without intergranular or cleavage modes.

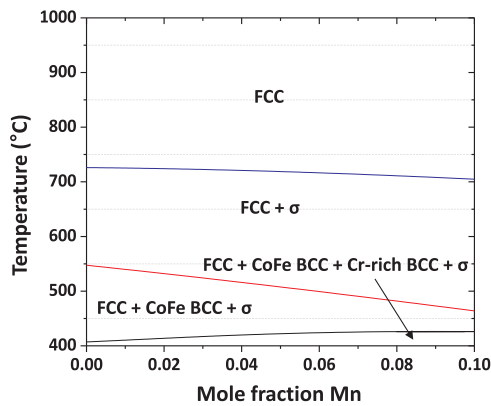


Fig. 7. Equilibrium phase fractions of 10V-15Cr-xMn-(40-x)Fe-10Co-25Ni alloys as a function of Mn content. The formation temperature of σ phase is underestimated than actual microstructure, but two phase region of fcc and σ increases as Mn content increases.

Table 2

Calculated formation parameters and criteria [9] of the 10V-15Cr-xMn-(40-x)Fe-10Co-25Ni HEAs.

| Alloy | δ | S | ΔH_{mix} | VEC |
|-----------|--------------|--------------|---|---|
| 0Mn | 4.13% | 1.46 R | − 5.29 kJ/mol | 8 |
| 5Mn | 4.15% | 1.61 R | − 5.66 kJ/mol | 7.95 |
| 10Mn | 4.17% | 1.68 R | − 6.03 kJ/mol | 7.9 |
| Criterion | $\leq 6.6\%$ | $\geq 1.6 R$ | $-15 \text{ kJ/mol} < \Delta H_{\text{mix}} < 5 \text{ kJ/mol}$ | FCC (VEC ≥ 8) BCC (VEC < 6.87) HCP (5.3 \leq VEC < 5.8) |

determining single-fcc-phase HEAs [17,27,29,56,57]. When all parameters except S are satisfied with the formation condition for single-fcc-phase HEAs in 0Mn, the VEC value is deviated from the HEA formation condition as the Mn content increases to 5–10 at%, which influences the formation of the σ phase, similar to the 10Mn alloy. Among the four parameters (δ , S, ΔH_{mix} , VEC), the VEC value decreases to below 8 in the 10Mn alloy, which might promote the formation of the σ phase, although the VEC value of 7.9 is slightly higher than the σ phase formation criterion [53–55].

It is interesting to note that the twinning tends to increase with increasing Fe content, as shown in Fig. 5a–f. In fcc alloys (such as austenitic steels, Cu alloys, and Al alloys), it has been reported that the deformation twinning is influenced by stacking fault energy (SFE), short range ordering, and friction stress, among which the SFE plays the

largest role [58–60]. The SFE (Γ) is expressed as follows [58]:

$$\Gamma = 2\rho\Delta G^{\text{fcc} \rightarrow \text{hcp}} + 2\sigma^{\text{fcc}/\text{hcp}} \quad (1)$$

where ρ , $\Delta G^{\text{fcc} \rightarrow \text{hcp}}$, and $\sigma^{\text{fcc}/\text{hcp}}$ are the molar surface density along the {111} planes, the free energy for fcc \rightarrow hcp transformation, and the fcc/hcp interfacial energy, respectively. It is assumed that the trend of the relative stability of the hcp phase with respect to the fcc phase, i.e. $\Delta G^{\text{fcc-hcp}}$, is similar to that of the formation behavior of the deformation twin, and that the Gibbs free energy difference between fcc and hcp, i.e. $G_{\text{fcc}} - G_{\text{hcp}}$, shows the same behavior as that of SFE. Thermodynamic calculations based on the present database are not accurate below 0 °C, but the 0 °C-calculations can be reasonably accepted for the stability evaluation at cryogenic temperature [61]. Thus, the calculations were carried out at 0 °C to estimate the effects of alloying elements on relative stability between the fcc and hcp phases. According to the calculation results (Fig. 1a–c), the database of the σ phase is somewhat insufficient, but the energy relationships between the solid solutions of fcc, bcc, and hcp are well established for this 6-component alloy system. The $\Delta G^{\text{fcc-hcp}}$ is calculated to be − 674.5, − 801.3, and − 894.1 J/mol for the 0Mn, 5Mn, and 10Mn alloys, respectively. This indicates that the fcc phase becomes more unstable as the Fe content increases, and that the stacking fault probability tends to increase, which is favorable for the deformation twinning. Thus, the number of twins increases with increasing Fe content, as confirmed in Fig. 5a–f.

The deformation twinning mechanism is also affected by the decreased grain size due to the Mn addition. The fcc grain size is reduced from 8.4 μm to 3.0 μm as the Mn content increases from 0 at% to 10 at%. This is influenced by the grain boundary pinning by the σ particle. The grain boundary pinning effect of the σ particle was verified experimentally in this study. When the 10Mn alloy is annealed at 950 °C and 1000 °C for 10 min, the grain size increases to 6.0 μm and 29.1 μm , respectively, as the σ particles disappear at the annealing temperature of 1000 °C (Fig. 8). This abrupt increase in grain size is attributed to the disappearance of the grain boundary pinning effect of the σ particles. Therefore, the grain size of the 10Mn alloy is much smaller (3.0 μm) than that of the 0Mn alloy (8.4 μm) because of the grain boundary pinning effect due to grain-boundary σ particles. Since the critical twinning stress increases with decreasing grain size, the decrease in the twinning amount with increasing Mn content is also closely related to the grain refinement.

Fig. 9 shows the difference between cryogenic-temperature tensile and yield strengths ($\Delta(\text{TS-YS})$), which have roughly the same trends as the strain-hardening effect [36], together with the calculated $\Delta G^{\text{fcc-hcp}}$ values. When the Mn content increases from 0% to 5%, the $\Delta G^{\text{fcc-hcp}}$ decreases, and the twinning also decreases, thereby resulting in a decrease in strain hardening. In the 10Mn alloy, decreased strain

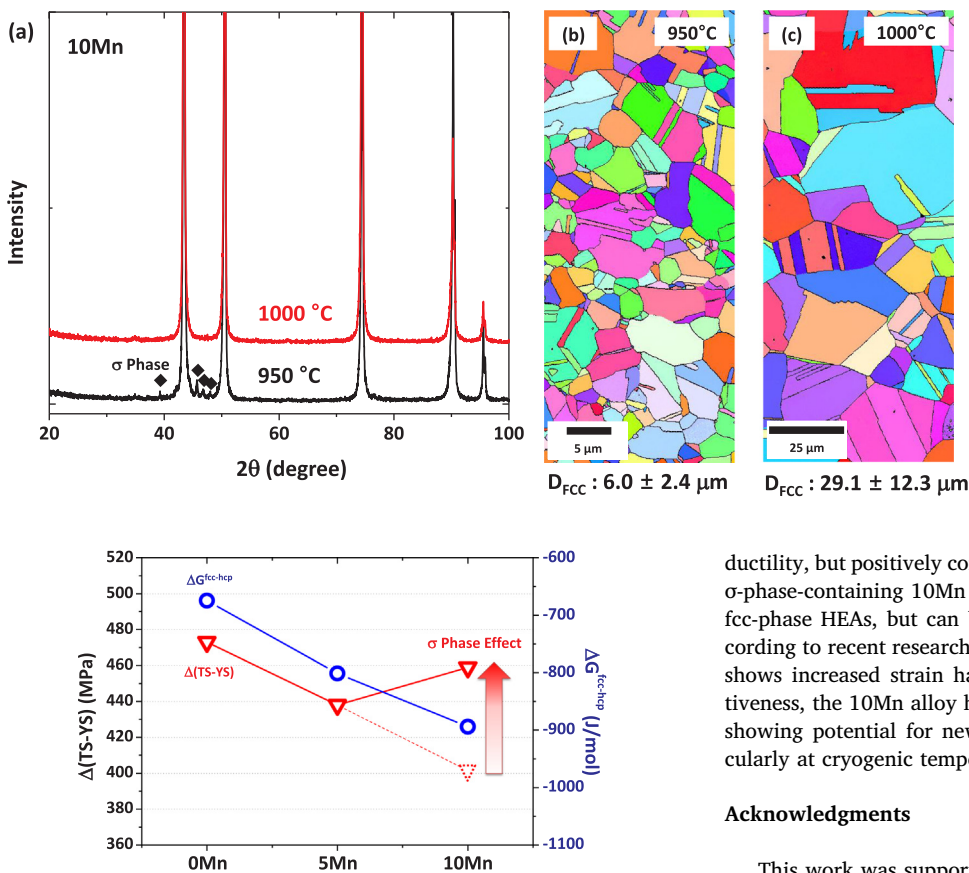


Fig. 9. Difference between cryogenic-temperature tensile and yield strengths ($\Delta(TS-YS)$). When the Mn content increases from 0 at% to 5 at%, the $\Delta G^{fcc-hcp}$ decreases, while the twinning decreases, thereby resulting in the decrease in strain hardening. In the 10Mn alloy, the decreased strain hardening might be expected (a red-dashed line) by the least twinning. However, the $\Delta(TS-YS)$ increases to 459 MPa (a red-solid line), while the elongation decreases to 54.1% which is lower than those of the 0Mn and 5Mn alloys. This is attributed to the σ -phase strengthening.

hardening might be expected (a red-dashed line in Fig. 9) due to the least twinning (Fig. 5c and f). However, the $\Delta(TS-YS)$ increases to 459 MPa (a red-solid line), while the elongation decreases to 54.1%, which is lower than those of the 0Mn and 5Mn alloys. The strain-hardening rate curves also show higher strain hardening in the 10Mn alloy than in the 0Mn and 5Mn alloys (Fig. 4b), despite the decreased $\Delta G^{fcc-hcp}$ and fine grain size due to pinning effects. This higher strain hardening is attributed to the σ -phase strengthening. These brittle intermetallic σ particles mostly lie along grain boundaries, but seldom initiate brittle intergranular or cleavage cracks because the adjacent fcc matrix is sufficiently ductile (Fig. 6a and b). Therefore, they favorably contribute to the improvement of strengths and strain hardening while the elongation deteriorates.

5. Conclusions

This study on the utilization of hard grain-boundary σ particles demonstrates a novel way to improve cryogenic-temperature tensile properties in the newly designed Fe-rich VCrMnFeCoNi HEAs. In the present 5- or 6-component non-equi-atomic HEAs, the increase in Fe plays an important role in more populated deformation twinning, while the Mn addition results in suppression of twinning and solid-solution hardening. In the 10Mn alloy, the σ particles are formed along the grain boundaries, which leads to further grain refinement due to grain boundary pinning and to the improvement in strain hardening despite the reduced twinning. This utilization of the σ phase leads to the loss of

ductility, but positively contributes to the improvement of strength. The σ -phase-containing 10Mn alloy is not classified into traditional single-fcc-phase HEAs, but can be regarded as a precipitation-type HEA according to recent research trends on HEAs. Since the Fe-rich 0Mn alloy shows increased strain hardening and ductility as well as cost-effectiveness, the 10Mn alloy has merits of excellent properties of strength, showing potential for new applications in high-strength HEAs, particularly at cryogenic temperature.

Acknowledgments

This work was supported by the Future Material Discovery Project of the National Research Foundation of Korea (NRF) funded by the Ministry of Science, ICT, and Future Planning (MSIP) of Korea (NRF-2016M3D1A1023383) and by Brain Korea 21 PLUS Project for Center for Creative Industrial Materials.

References

- [1] O.N. Senkov, G.B. Wilks, J.M. Scott, D.B. Miracle, Mechanical properties of Nb₂₅Mo₂₅Ta₂₅W₂₅ and V₂₀Nb₂₀Mo₂₀Ta₂₀W₂₀ refractory high entropy alloys, *Intermetallics* 19 (2011) 698–706.
- [2] M.S. Lucas, G.B. Wilks, L. Mauger, J.A. Muñoz, O.N. Senkov, E. Michel, J. Horwath, S.L. Semiatin, M.B. Stone, D.L. Abernathy, E. Karapetrova, Absence of long-range chemical ordering in equimolar FeCoCrNi, *Appl. Phys. Lett.* 100 (2012) 251907.
- [3] Z. Wu, H. Bei, F. Otto, G.M. Pharr, E.P. George, Recovery, recrystallization, grain growth and phase stability of a family of FCC-structured multi-component equiatomic solid solution alloys, *Intermetallics* 46 (2014) 131–140.
- [4] R. Kozak, A. Sologubenko, W. Steurer, Single-phase high-entropy alloys – an overview, *Z. Krist.* 230 (2015) 55–68.
- [5] O.N. Senkov, S.V. Senkova, C. Woodward, D.B. Miracle, Low-density, refractory multi-principal element alloys of the Cr–Nb–Ti–V–Zr system: microstructure and phase analysis, *Acta Mater.* 61 (2013) 1545–1557.
- [6] X. Yang, Y. Zhang, P.K. Liaw, Microstructure and compressive properties of NbTiVAlx high entropy alloys, *Procedia Eng.* 36 (2012) 292–298.
- [7] J.-W. Yeh, S.-K. Chen, S.-J. Lin, J.-Y. Gan, T.-S. Chin, T.-T. Shun, C.-H. Tsau, S.-Y. Chang, Nanostructured high-entropy alloys with multiple principal elements: novel alloy design concepts and outcomes, *Adv. Eng. Mater.* 6 (2004) 299–303.
- [8] K.M. Youssef, A.J. Zaddach, C. Niu, D.L. Irving, C.C. Koch, A novel low-density, high-hardness, high-entropy alloy with close-packed single-phase nanocrystalline structures, *Mater. Res. Lett.* 3 (2015) 95–99.
- [9] Y. Zhang, T.T. Zuo, Z. Tang, M.C. Gao, K.A. Dahmen, P.K. Liaw, Z.P. Lu, Microstructures and properties of high-entropy alloys, *Prog. Mater. Sci.* 61 (2014) 1–93.
- [10] M.H. Tsai, J.-W. Yeh, High-entropy alloys: a critical review, *Mater. Res. Lett.* 2 (2014) 107–123.
- [11] B. Cantor, I.T.H. Chang, P. Knight, A.J.B. Vincent, Microstructural development in equiatomic multicomponent alloys, *Mater. Sci. Eng. A* 375 (2004) 213–218.
- [12] F. Otto, A. Dlouhý, Ch Somsen, H. Bei, G. Eggeler, E.P. George, The influences of temperature and microstructure on the tensile properties of a CoCrFeMnNi high-entropy alloy, *Acta Mater.* 61 (2013) 5743–5755.
- [13] B. Gludovatz, A. Hohenwarter, D. Catoor, E.H. Chang, E.P. George, O.R. Robert, A fracture-resistant high-entropy alloy for cryogenic applications, *Science* 345 (2014) 1153–1158.
- [14] G. Laplanche, A. Kostka, O.M. Horst, G. Eggeler, E.P. George, Microstructure

- evolution and critical stress for twinning in the CrMnFeCoNi high-entropy alloy, *Acta Mater.* 118 (2016) 152–163.
- [15] O.N. Senkov, G.B. Wilks, D.B. Miracle, C.P. Chuang, P.K. Liaw, Refractory high-entropy alloys, *Intermetallics* 18 (2010) 1758–1765.
 - [16] Y.X. Zhuang, W.J. Liu, Z.Y. Chen, H.D. Xue, J.C. He, Effect of elemental interaction on microstructure and mechanical properties of FeCoNiCuAl alloys, *Mater. Sci. Eng. A* 556 (2012) 395–399.
 - [17] M.J. Yao, K.G. Pradeep, C.C. Tasan, D. Raabe, A novel, single phase, non-equiatomic FeMnNiCoCr high-entropy alloy with exceptional phase stability and tensile ductility, *Scr. Mater.* 72–73 (2014) 5–8.
 - [18] D. Li, C. Li, T. Feng, Y. Zhang, G. Sha, J.J. Lewandowski, P.K. Liaw, Y. Zhang, High-entropy $\text{Al}_{0.5}\text{CoCrFeNi}$ alloy fibers with high tensile strength and ductility at ambient and cryogenic temperatures, *Acta Mater.* 123 (2017) 285–294.
 - [19] J.Y. He, H. Wang, H.L. Huang, X.D. Xu, M.W. Chen, Y. Wu, X.J. Liu, T.G. Nieh, K. An, Z.P. Lu, A precipitation-hardened high-entropy alloy with outstanding tensile properties, *Acta Mater.* 102 (2016) 187–196.
 - [20] W.H. Liu, Z.P. Lu, J.Y. He, J.H. Luan, Z.J. Wang, B. Liu, Yong Liu, M.W. Chen, C.T. Liu, Ductile CoCrFeNiMox high entropy alloys strengthened by hard inter-metallic phases, *Acta Mater.* 116 (2016) 332–342.
 - [21] Z. Wu, C.M. Parish, H. Bei, Nano-twin mediated plasticity in carbon-containing FeNiCoCrMn high entropy alloys, *J. Alloy. Compd.* 647 (2015) 815–822.
 - [22] Z. Wang, I. Baker, Z. Cai, S. Chen, J.D. Poplawsky, W. Guo, The effect of interstitial carbon on the mechanical properties and dislocation substructure evolution in Fe₄₀Ni_{11.3}Mn_{34.8}Al_{7.5}Cr₆ high entropy alloys, *Acta Mater.* 120 (2016) 228–239.
 - [23] K.B. Zhang, Z.Y. Fu, J.Y. Zhang, W.M. Wang, H. Wang, Y.C. Wang, Q.J. Zhang, J. Shi, Microstructure and mechanical properties of CoCrFeNiTiAlx high-entropy alloys, *Mater. Sci. Eng. A* 508 (2009) 214–219.
 - [24] S. Varalakshmi, M. Kamaraj, B.S. Murty, Formation and stability of equiatomic and nonequiatomic nanocrystalline CuNiCoZnAlTi high-entropy alloys by mechanical alloying, *Metall. Mater. Trans. A* 41 (2010) 2703–2709.
 - [25] C. Li, J.C. Li, M. Zhao, Q. Jiang, Effect of alloying elements on microstructure and properties of multiprincipal elements high-entropy alloys, *J. Alloy. Compd.* 475 (2009) 752–757.
 - [26] Y. Zhang, Y.J. Zhou, J.P. Lin, G.L. Chen, P.K. Liaw, Solid-solution phase formation rules for multi-component alloys, *Adv. Eng. Mater.* 10 (2008) 534–538.
 - [27] D. Ma, M. Yao, K.G. Pradeep, C.C. Tasan, H. Springer, D. Raabe, Phase stability of non-equiatomic CoCrFeMnNi high entropy alloys, *Acta Mater.* 98 (2015) 288–296.
 - [28] X. Xian, Z. Zhong, B. Zhang, K. Song, C. Chen, S. Wang, J. Cheng, Y. Wu, A high-entropy V₃₅Ti₃₅Fe₁₅Cr₁₀Zr₅ alloy with excellent high-temperature strength, *Mater. Des.* 121 (2017) 229–236.
 - [29] K.G. Pradeep, C.C. Tasan, M.J. Yao, Y. Deng, H. Springer, D. Raabe, Non-equiatomic high entropy alloys: approach towards rapid alloy screening and property-oriented design, *Mater. Sci. Eng. A* 648 (2015) 183–192.
 - [30] Z. Li, K.G. Pradeep, Y. Deng, D. Raabe, C.C. Tasan, Metastable high-entropy dual-phase alloys overcome the strength–ductility trade-off, *Nature* 534 (2016) 227–230.
 - [31] B. Gludovatz, A. Hohenwarter, K.V.S. Thurston, H. Bei, Z. Wu, E.P. George, R.O. Ritchie, Exceptional damage-tolerance of a medium-entropy alloy CrCoNi at cryogenic temperatures, *Nat. Commun.* 7 (2016) 10602.
 - [32] C.-Y. Hsu, T.-S. Sheu, J.-W. Yeh, S.-K. Chen, Effect of iron content on wear behavior of AlCoCrFeMo_{0.5}Ni high-entropy alloys, *Wear* 268 (2010) 653–659.
 - [33] D. Raabe, C.C. Tasan, H. Springer, M. Bausch, From high-entropy alloys to high entropy steels, *Steel Res. Int.* 86 (2015) 1127–1138.
 - [34] Y.H. Jo, S. Jung, W.M. Choi, S.S. Sohn, H.S. Kim, B.J. Lee, N.J. Kim, S. Lee, Cryogenic strength improvement by utilizing room-temperature deformation twinning in a partially recrystallized VCrMnFeCoNi high-entropy alloy, *Nat. Commun.* 8 (2017) 15719.
 - [35] A. Gali, E.P. George, Tensile properties of high-and medium-entropy alloys, *Intermetallics* 39 (2013) 74–78.
 - [36] Z. Wu, H. Bei, G.M. Pharr, E.P. George, Temperature dependence of the mechanical properties of equiatomic solid solution alloys with face-centered cubic crystal structures, *Acta Mater.* 81 (2014) 428–441.
 - [37] W.C. Oliver, G.M. Pharr, An improved technique for determining hardness and elastic modulus using load and displacement sensing indentation experiments, *J. Mater. Res.* 7 (1992) 1564–1583.
 - [38] F.R. de Boer, R. Boom, W.C.M. Mattens, A.R. Miedema, A.K. Niessen, *Cohesion in Metals: Transition Metal Alloys*, North-Holland, Amsterdam, Netherlands, 1988.
 - [39] B. Sundman, B. Jansson, J.O. Andersson, The thermo-calc databank system, *Calphad* 9 (1985) 153–190.
 - [40] B.J. Lee, B. Sundman, *TCFE2000: The Thermo-Calc Steels Database*, KTH, Stockholm, 1999.
 - [41] K.G. Chin, H.J. Lee, J.H. Kwak, J.Y. Kang, B.J. Lee, Thermodynamic calculation on the stability of (Fe, Mn)₃AlC carbide in high aluminum steels, *J. Alloy. Compd.* 505 (2010) 217–223.
 - [42] W.-M. Choi, S. Jung, Y.H. Jo, S. Lee, B.-J. Lee, Design of new face-centered cubic high entropy alloys by thermodynamic calculation, *Met. Mater. Int.* 23 (2017) 839–847.
 - [43] J.C. Williams, E.A. Starke, Progress in structural materials for aerospace systems, *Acta Mater.* 51 (2003) 5775–5799.
 - [44] R.C. Reed, Z. Zhu, A. Sato, D.J. Crudden, Isolation and testing of new single crystal superalloys using alloys-by-design method, *Mater. Sci. Eng. A* 667 (2016) 261–278.
 - [45] D.B. Miracle, J.D. Miller, O.N. Senkov, C. Woodward, M.D. Uchic, J. Tiley, Exploration and development of high entropy alloys for structural applications, *Entropy* 16 (2014) 494–525.
 - [46] S.M. Dubiel, J. Cieślak, Sigma-phase in Fe-Cr and Fe-V alloy systems and its physical properties, *Crit. Rev. Sol. Stat. Mater. Sci.* 36 (2011) 191–217.
 - [47] B.J. Lee, D.N. Lee, A thermodynamic study on the V-C and Fe-V systems, *Calphad* 15 (1991) 283–291.
 - [48] J. Michalska, M. Sozanska, Effect of intermetallic precipitations on the properties of duplex stainless steel, *Mater. Charact.* 56 (2006) 355–362.
 - [49] C.-C. Hsieh, W. Wu, Overview of intermetallic sigma (σ) phase precipitation in stainless steels, *ISRN Metall.* 2012 (2012) 1–16.
 - [50] M.C. Gao, J.-W. Yeh, P.K. Liaw, Y. Zhang, *High-Entropy Alloys: Fundamentals and Applications*, Springer, Cham, Switzerland, 2016.
 - [51] F. Otto, A. Dlouhý, K.G. Pradeep, M. Kuběnová, D. Raabe, G. Eggeler, E.P. George, Decomposition of the single-phase high-entropy alloy CrMnFeCoNi after prolonged anneals at intermediate temperatures, *Acta Mater.* 112 (2016) 40–52.
 - [52] M.J. Jang, S.-H. Joo, C.-W. Tsai, J.-W. Yeh, H.S. Kim, Compressive deformation behavior of CrMnFeCoNi high-entropy alloy, *Met. Mater. Int.* 22 (2016) 982–986.
 - [53] G.A. Salishchev, M.A. Tikhonovsky, D.G. Shaysultanov, N.D. Stepanov, A.V. Kuznetsov, I.V. Kolodiy, A.S. Tortika, O.N. Senkov, Effect of Mn and V on structure and mechanical properties of high-entropy alloys based on CoCrFeNi system, *J. Alloy. Compd.* 591 (2014) 11–21.
 - [54] N.D. Stepanov, D.G. Shaysultanov, G.A. Salishchev, M.A. Tikhonovsky, E.E. Oleynik, A.S. Tortika, O.N. Senkov, Effect of V content on microstructure and mechanical properties of the CoCrFeMnNi_x high entropy alloys, *J. Alloy. Compd.* 628 (2015) 170–185.
 - [55] M.-H. Tsai, K.-Y. Tsai, C.-W. Tsai, C. Lee, C.-C. Juan, J.-W. Yeh, Criterion for sigma phase formation in Cr- and V-containing high entropy alloys, *Mater. Res. Lett.* 1 (2013) 207–212.
 - [56] Z. Cai, X. Cui, G. Jin, Z. Liu, W. Zheng, Y. Li, L. Wang, Microstructure and thermal stability of a Ni-Cr-Co-Ti-V-Al high-entropy alloy coating by laser surface alloying, *Met. Mater. Int.* 23 (2017) 1012–1018.
 - [57] H.J. Park, Y.S. Na, S.H. Hong, J.T. Kim, Y.S. Kim, K.R. Lim, J.M. Park, K.B. Kim, Phase evolution, microstructure and mechanical properties of equi-atomic substituted TiZrHfNiCu and TiZrHfNiCuM (M = Co, Nb) high-entropy alloys, *Met. Mater. Int.* 22 (2016) 551–556.
 - [58] S. Curtze, V.-T. Kuokkala, Dependence of tensile deformation of TWIP steels on stacking fault energy, temperature and strain rate, *Acta Mater.* 58 (2010) 5129–5141.
 - [59] K.-T. Park, K.G. Jin, S.H. Han, S.W. Hwang, K. Choi, C.S. Lee, Stacking fault energy and plastic deformation of fully austenitic high manganese steels: effect of Al addition, *Mater. Sci. Eng. A* 527 (2010) 3651–3661.
 - [60] I. Karaman, H. Sehitoglu, K. Gall, Y.I. Chumlyakov, H.J. Maier, Deformation of single crystal hadfield steel by twinning and slip, *Acta Mater.* 48 (2000) 1345–1359.
 - [61] S.S. Sohn, S. Hong, J. Lee, B.-C. Suh, S.-K. Kim, B.-J. Lee, N.J. Kim, S. Lee, Effects of Mn and Al contents on cryogenic-temperature tensile and Charpy impact properties in four austenitic high-Mn steels, *Acta Mater.* 100 (2015) 39–52.